International Journal of Mechanical Sciences 312 (2026) 111223

Contents lists available at ScienceDirect

International Journal of Mechanical Sciences

journal homepage: www.elsevier.com/locate/ijmecsci

Hierarchical metamaterial with auxetic foams for low-frequency seismic attenuation

Jiazhen Zhang [a], Chaoyang Zhao [a], Guobiao Hu [b,*], Dewen Yu [c,d], Xingbo Pu [e], Yaowen Yang [a,*]

[a] School of Civil and Environmental Engineering, Nanyang Technological University, Nanyang Avenue 639798, Singapore
[b] Internet of Things Thrust, The Hong Kong University of Science and Technology (Guangzhou), Guangzhou 511400, China
[c] Frontier Institute of Science and Technology, Xi'an Jiaotong University, Xi'an 710049, China
[d] Key Laboratory of Education Ministry for Modern Design and Rotor-Bearing System, School of Mechanical Engineering, Xi'an Jiaotong University, Xi'an 710049, China
[e] Department of Civil and Environmental Engineering, The Hong Kong Polytechnic University, Hong Kong, China

ARTICLE INFO

Keywords:
Seismic metamaterials
Wave suppression
Band gap
Hierarchical structures
Negative Poisson's ratio
Complex band structure

ABSTRACT

Seismic metamaterials (SMs) show immense potential for vibration mitigation, yet challenges remain in achieving ultra-low-frequency and broadband attenuation. This paper proposes a hierarchical SM design incorporating auxetic foams with negative Poisson's ratio (NPR), capable of attenuating both Lamb and surface waves. For Lamb wave attenuation, the hierarchical NPR-based SM is developed and analyzed using the finite element method in conjunction with the $k(\omega)$ technique. Computed complex band structures reveal the presence of evanescent modes, downward-shifted band gaps, and additional band gaps induced by hierarchical resonances. For surface wave attenuation, a second SM configuration integrates a square section within the NPR-based hierarchical unit cell, enabling the emergence of negative effective mass and the formation of continuous, ultra-low-frequency band gaps below 29 Hz. Finite element simulations verify the attenuation performance in both frequency and time domains. The analysis further elucidates how hierarchical arrangement facilitates multi-scale resonances and how the negative effective mass mechanism suppresses surface wave modes within attenuation zones. Time-domain simulations under seismic excitations from the El Centro and Taft records demonstrate substantial ground motion attenuation, achieving RMS acceleration reductions of 90.93% and 84.12%, respectively, at the top of a 10-story steel frame structure. Laboratory-scale experiments further validate these numerical results, confirming a superior suppression performance enabled by the negative effective mass effect. These findings highlight the practical potential of hierarchical NPR-based seismic metamaterials in enhancing the seismic resilience of large-scale infrastructure.

1. Introduction

Metamaterials composed of periodic unit cells exhibiting unique band gap phenomena—frequency ranges in which wave propagation is inhibited—have been extensively investigated over the past decades for vibration suppression and control [1–4]. Owing to their superior efficiency in attenuating vibrations, seismic metamaterials (SMs) have emerged as a promising solution for earthquake-resistant building design [5–8]. Unlike conventional approaches that employ mass dampers or rubber isolators to attenuate structural vibrations [9–12], SMs mitigate seismic risk by impeding wave propagation before it impacts the building.

From the formation mechanism perspective, band gaps are generally classified into two types: locally resonant (LR) band gaps [13–16] and Bragg scattering (BS) band gaps [17–20]. However, the practical application of SMs is hindered by two major challenges: the typically narrow bandwidths of the band gaps and their relatively high operating frequency ranges. To overcome these limitations, various strategies have been proposed. Inspired by sound attenuation observed in jungles [21], trees were deemed natural SMs and investigated for their ability to reduce low-frequency vibrations [22–24]. Zhang et al. [25] proposed SMs composed of cross-shaped and square steel sections capable of attenuating Lamb waves below 20 Hz. Built-up structural steel sections were also proposed to suppress low-frequency seismic waves by

* Corresponding authors.
E-mail addresses: guobiaohu@hkust-gz.edu.cn (G. Hu), cywyang@ntu.edu.sg (Y. Yang).

https://doi.org/10.1016/j.ijmecsci.2026.111223
Received 23 September 2025; Received in revised form 23 December 2025; Accepted 6 January 2026
Available online 8 January 2026

leveraging LR band gaps [26]. Gao et al. [27] combined LR and BS mechanisms to broaden the attenuation zone. Subsequently, an embedded SM was designed with an ultra-low-frequency band gap, characterized by the absence of surface wave solutions in the 0-16.3 Hz range [28]. In a more recent study, Wang et al. [29] utilized the negative effective mass density mechanism to open a zero-frequency band gap; however, vibrational mode analysis was not provided to substantiate their findings. Additionally, materials with a negative Poisson's ratio (NPR) have attracted growing interest in SM design, due to their auxetic behavior—lateral expansion/contraction in response to tensile/compressive loading [30]. Building upon pioneering efforts that used NPR foams to suppress Lamb waves [31] and surface waves [32], Li et al. [33] developed NPR-based SMs capable of achieving ultra-wide, low-frequency attenuation for both wave types. Nonetheless, several advanced strategies that have been widely explored in conventional metamaterials to widen bandwidths in the low-frequency domain remain underexplored in SMs, including the incorporation of nonlinearities [34–37], the acoustic black hole effect [38–41], and structural hierarchy [42–45].

Natural materials such as wood and bone have evolved over millions of years to exhibit extraordinary mechanical properties tailored to their environmental conditions. One of the key contributors to these exceptional properties is their hierarchical micro-structural organization [46,47], which has drawn significant interest. Hierarchically structured materials demonstrate enhanced attributes, including a favorable combination of light weight and high stiffness [48], superior damage tolerance [49], and high energy absorption capacity [50]. Zhang et al. [51] were among the first to apply hierarchical design in metamaterials, successfully generating additional band gaps. Since then, hierarchical metamaterials have been explored for vibration attenuation and energy absorption [52]. A bioinspired honeycomb hierarchical metamaterial was designed to suppress elastic waves at subwavelength scales [53], and lightweight hierarchical designs were developed to produce multiple wide band gaps in the high-frequency regime [54]. Jing et al. [55] analyzed band gaps in hierarchical phononic crystals and categorized them based on vibration patterns. Despite these advances, the application of hierarchical design in SMs remains limited. Miniaci et al. [56] proposed the first hierarchical SM; however, the resulting band gaps were narrow and sporadically distributed. More recently, a hierarchical SM for multidirectional wave suppression was reported [57], yet the study lacked a detailed analysis of band gap formation mechanisms and time-domain validation.

Current SM research predominantly relies on the finite element (FE) method [58–62] to compute the dispersion relations of propagating waves. However, evanescent waves, which play a crucial role in mode conversion, are always neglected in such analyses. To address this limitation, the $k(\omega)$ technique in the plane wave expansion (PWE) method [63] offers a viable approach for capturing these overlooked wave components. When integrated with the FE framework, the $k(\omega)$ method enables the characterization of the relationship between real frequencies and complex wave numbers in periodic structures [64–67]. In the conventional $\omega(k)$ approach, eigenvalue problems are solved for unknown frequencies (ω) at given real wave numbers (k), yielding only real band structures. In contrast, $k(\omega)$ technique adopts an inverse formalism, in which wave numbers (k) are computed for given real frequencies (ω). This formulation facilitates the derivation of complex band structures, where evanescent waves appear and serve to connect propagating modes at the boundaries of attenuation zones [68]. As a result, complex band structures offer critical insights into the transition between propagating and non-propagating wave modes and reveal the physical mechanisms underlying band gap formation [42,69].

Another essential aspect of SM research is the validation of wave attenuation. Wang et al. [70] conducted a laboratory-scale experiment employing foam pads and cardboard to impose low boundary conditions. A more recent experimental study [71] detailed the fabrication process of NPR-based SMs; however, significant discrepancies were observed between the experimental and FE simulation results. Moreover, classical seismic wave data, such as the Taft and El Centro records from the PEER Ground Motion Database, are often used in time-domain simulations for validation [72–75]. While comparisons of ground accelerations before and after SM implementation demonstrate attenuation effectiveness, the structural response of buildings is seldom considered. For instance, Wen et al. [76] proposed a multi-resonator elastic metamaterial with the basement acting as the SM. While real earthquake signals were used to compare top-floor displacements, the seismic influences on buildings were not convincingly demonstrated, as the building was oversimplified.

To address the aforementioned research gaps, this study proposes a hierarchical SM that integrates the auxetic foam (abbreviated as "NPR-based" in later sections) and negative effective mass density mechanisms for ultra-low-frequency and broadband seismic vibration attenuation. In this study, the term 'NPR' refers to the intrinsic negative Poisson's ratio of the auxetic foam used as the coating material of the unit cell, rather than the effective Poisson's ratio of the overall metamaterial structure. A FE model based on the $k(\omega)$ technique is developed to comprehensively characterize band gap formation and the underlying mechanisms.

This paper is structured into four sections. Following the introduction in Section 1, Section 2 details the geometry and material properties of the proposed SM for Lamb wave attenuation, along with the implementation of the FE method for complex band structure analysis. Band gap formation is discussed by analyzing complex band structures and vibrational modes, followed by a frequency-domain transmittance analysis. Section 3 presents the wave suppression efficiency of SM under surface waves, along with the frequency- and time-domain analyses, with particular emphasis on its practical implications for structural engineering. A laboratory-scale experimental study is conducted following parametric analysis. Finally, Section 4 summarizes the key findings and highlights the primary advantages of the proposed hierarchical SM.

2. Wave suppression for lamb wave

Seismic waves arise from the superposition of bulk and surface waves propagating in complex near-surface environments. In layered media, seismic energy may become partially confined within a finite-thickness layer, giving rise to guided wave modes whose dispersion characteristics can be well approximated by Lamb waves. Although Lamb waves are based on an idealized plate model, they provide a useful and widely adopted framework for analyzing near-surface guided wave propagation. Accordingly, Lamb waves are employed in this work as an idealized benchmark to elucidate the attenuation mechanisms of the proposed seismic metamaterial, prior to extending the analysis to physically realistic half-space surface waves. This section presents a comprehensive overview of the structural design and computational methodology employed to obtain the complex band structure of the proposed SMs for Lamb wave attenuation. Further, a frequency-domain transmittance is calculated to validate Lamb wave attenuation efficiency.

2.1. Models and methods

Fig. 1 illustrates the schematic of the proposed NPR-based hierarchical SMs. The NPR-based single unit cell and the rubber-based hierarchical unit cell are shown in Fig. 1(b) and (d), respectively. The unit cell (Fig. 1(b)), representing the first hierarchical level, has a length of L_a, whereas the unit cell depicted in Fig. 1(c), corresponding to the second-level hierarchical configuration, has a length of L. The outer side lengths of the steel filler and the concrete core are denoted by L_b and L_c, respectively. The thickness of the auxetic foam can be calculated as $(L_a - L_b)/2$. The height t remains constant across all SM configurations.

As mentioned before, the FE method employing the $k(\omega)$ technique can be used to compute the complex band structure of periodic structures. Assuming the SM extends infinitely, Bloch's theorem is applied to account for structural periodicity. The computation is performed using a

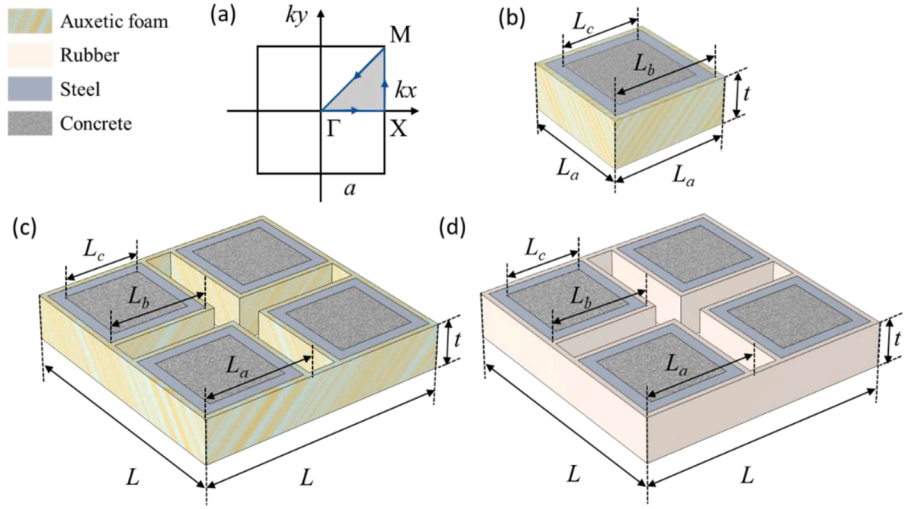

Fig. 1. Schematic of (a) first irreducible Brillouin zone, and proposed SMs for Lamb wave suppression: (b) an NPR-based unit cell, representing first hierarchical level in (c) an NPR-based hierarchical unit cell with two hierarchical levels, (d) a rubber-based hierarchical unit cell.

corresponding FE model established within the Partial Differential Equation (PDE) module of the commercial software COMSOL Multiphysics. The governing PDE is expressed as follows:

$$e_a\Lambda^2 U - d_a\Lambda^2 U - \nabla\cdot(c:\nabla U + \alpha\cdot U - \gamma) + b\cdot U - \beta\cdot\nabla U = f, \tag{1}$$

where e_a and d_a, denote the mass and damping coefficients, respectively. α and β are the conservative flux convection coefficient and convection coefficient, respectively. c and b represent diffusion and absorption coefficients. γ is the conservative flux source term, and f is the source term. Λ represents the eigenvalue, and U is the eigenmode corresponding to Λ.

According to Bloch's theorem, any translation along the lattice constant a in the periodic plane is also periodic,

$$\psi(r) = e^{ika}U(r) = e^{ikr}\psi_k(r)U(r+a), \tag{2}$$

where $\Psi(r)$ denotes the periodic coordinate. Considering a harmonic wave propagates in the elastic solid without damping and source term, the Bloch wave can be written as:

$$\nabla\cdot[C(r):\nabla u] - \rho(r)\frac{\partial^2 u}{\partial t^2} = 0. \tag{3}$$

where u is the displacement. $C(r)$ and $\rho(r)$ represent the elastic tensor and mass density tensor of a position vector r, respectively. Combining Eqs.(2) and (3), the inverse formalism of the eigenvalue problem can be written as:

$$\begin{aligned}&(\nabla+\mathrm{i}k)\cdot\mu(r)(\nabla+\mathrm{i}k)u_{lk}(r) + (\nabla+\mathrm{i}k)\cdot[\mu(r)(\nabla+\mathrm{i}k)_l u_k(r)]\\ &+(\nabla+\mathrm{i}k)_l\lambda(r)(\nabla+\mathrm{i}k)\cdot u_k(r) + \rho(r)\omega^2 u_{lk}(r) = 0.\end{aligned} \tag{4}$$

As the eigenvalue $\Lambda = -\,\mathrm{i}k$, the coefficients in Eq. (1) can be calculated correspondingly:

$$c = \begin{bmatrix} \begin{bmatrix}\lambda+2\mu & 0\\ 0 & \mu\end{bmatrix} & \begin{bmatrix}0 & \lambda\\ \mu & 0\end{bmatrix}\\ \begin{bmatrix}0 & \mu\\ \lambda & 0\end{bmatrix} & \begin{bmatrix}\mu & 0\\ 0 & \lambda+2\mu\end{bmatrix}\end{bmatrix}, \tag{5}$$

$$e_a = \begin{bmatrix}-(\lambda+2\mu) & 0\\ 0 & -\mu\end{bmatrix}, \tag{6}$$

$$\alpha = \begin{bmatrix} \begin{bmatrix}(\lambda+2\mu)ik\\ 0\end{bmatrix} & \begin{bmatrix}0\\ \mu ik\end{bmatrix}\\ \begin{bmatrix}0\\ \lambda ik\end{bmatrix} & \begin{bmatrix}\lambda ik\\ 0\end{bmatrix}\end{bmatrix}, \tag{7}$$

$$\beta = \begin{bmatrix} [-(\lambda+2\mu)\mathrm{i}k & 0] & [0 & -\lambda\mathrm{i}k]\\ [0 & -\mu\mathrm{i}k] & [-\mu\mathrm{i}k & 0]\end{bmatrix}, \tag{8}$$

$$b = \begin{bmatrix}-\rho\omega^2 & 0\\ 0 & -\rho\omega^2\end{bmatrix}. \tag{9}$$

In the above equations, λ and μ represent the first and second Lame constants, respectively. While the complex band structure can be obtained by selecting the eigenvalue Λ and sweeping the frequency ω of interest, the real dispersion relation can be computed using the Structural Mechanics (Solid) module in COMSOL by sweeping the real wave numbers along the M–Γ–X–M path in the first irreducible Brillouin zone, as shown in Fig. 1(a).

2.2. Band structures and band gap formation mechanisms

Table 1 lists the material parameters used for the proposed SMs. The corresponding geometric parameters are: $L = 1.125$ m, $L_a = 0.5$ m, $L_b = 0.45$ m, $L_c = 0.35$ m, and $t = 0.2$ m. Fig. 2 presents the dispersion relations of the SMs configurations shown in Fig. 1, with band gaps highlighted in light blue. Notably, the frequency spectrum can be categorized into main propagative and attenuative regions, with the band gaps corresponding to attenuative zones and the remaining frequency ranges with real solutions indicating propagative regions [42]. This distinction is particularly evident in Fig. 2(b) and (c), where propagative and attenuative regions appear in an alternating manner.

Table 1
Material parameters of proposed SMs.

Material	Young's modulus (Pa)	Poisson's ratio	Density (kg/m^3)
Auxetic foam	2.5×10^4	-0.8	120
Rubber	1.05×10^5	0.47	1300
Steel	2.07×10^{11}	0.3	7850
Concrete	4×10^{10}	0.3	2500
Soil	2×10^7	0.3	1800

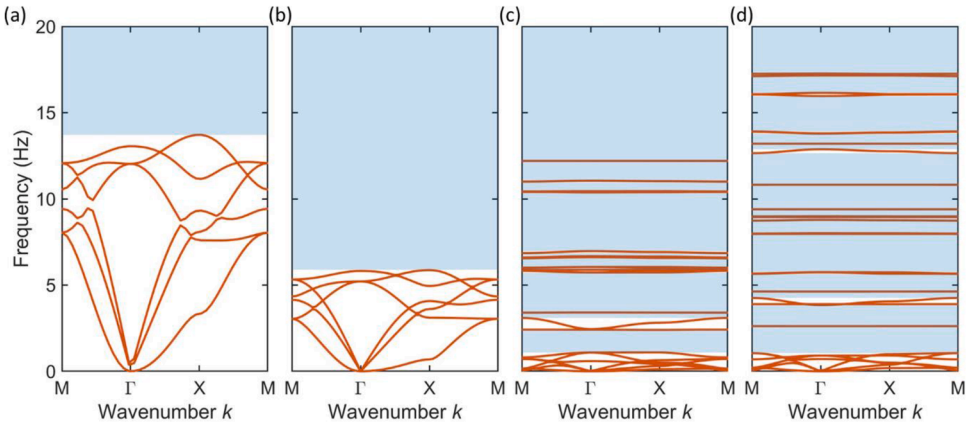

Fig. 2. Band structures of proposed SMs. (a) NPR-based SM with length of L_a showing no band gaps below 14 Hz. (b) NPR-based SM with length of L showing no band gaps below 6 Hz. (c) Hierarchical NPR-based SM exhibiting three main low-frequency attenuation regions ([1.09, 2.40] Hz, [3.10, 5.73] Hz, [6.05, 6.60] Hz), demonstrating effective low-frequency vibration suppression. (d) Rubber-based hierarchical SM with discontinuous and fragmented attenuation regions.

As depicted in Fig. 2(a) and (b), the single NPR-based SMs with the length of L_a and L do not exhibit any band gaps below 14 Hz and 6 Hz, respectively. In contrast, the hierarchical NPR-based SM displays three main attenuative regions in the low-frequency range, covering the frequency ranges [1.09, 2.40] Hz, [3.10, 5.73] Hz, and [6.05, 6.60] Hz. This suggests that hierarchical arrangement is effective in suppressing the low-frequency vibration. Furthermore, comparing Fig. 2(b) and (c) reveals that the rubber-based SM generates a greater number of dispersion curves, corresponding to propagating waves between the band gaps. Although the first attenuation region in the rubber-based SM spans 2.79 Hz, which is wider than the 1.31 Hz span of the first attenuation region in the NPR-based SM, the attenuation zones in Fig. 2(b) appear more continuous and better connected across the frequency spectrum. This indicates that the NPR-based SM supports broader and uninterrupted broadband attenuation, thereby enhancing broadband vibration suppression.

The complex band structures obtained using the FE method with the $k(\omega)$ technique are presented in Fig. 3. In the imaginary part of the complex band structure calculated from the PDE module for the NPR-based SM with the length of L_a (Fig. 3(a)), an evanescent mode branch that connects the upper and lower boundaries of the band gap (points A and B) is observed. A similar evanescent mode is observed in Fig. 3(b), linking points C and D. However, the complex band structure of the NPR-based hierarchical SM, depicted in Fig. 3(b), exhibits a more intricate pattern, with multiple branches of evanescent modes connecting band gaps. This complexity suggests that introducing hierarchical resonant elements at different scales leads to the formation of additional band gaps. Further insights are provided by the vibrational modes E and F, shown in Fig. 4, which reveal that only the connecting regions between the single elements undergo vibration. These

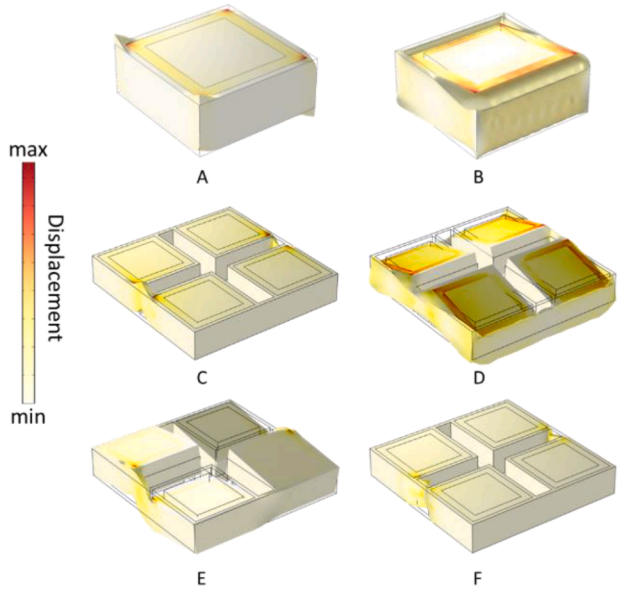

Fig. 4. Vibration modes of NPR-based single and hierarchical SMs of six points in Fig. 3.

connections, absent in the non-hierarchical SM, function as additional resonators in the hierarchical configuration. Their presence introduces new localized resonances, thereby contributing to the formation of extra band gaps. As depicted in Fig. 4, mode A exhibits edge vibrations around

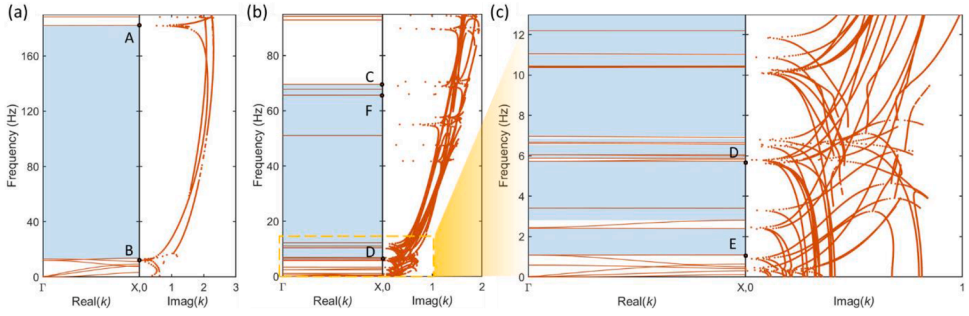

Fig. 3. Complex band structures of proposed SMs obtained using the FE method with the $k(\omega)$ technique. (a) NPR-based SM showing an evanescent mode connecting the upper and lower band gap boundaries. (b) NPR-based hierarchical SM exhibiting multiple evanescent branches linking band gaps. (c) Enlarged view of (b) highlighting the intricate pattern of hierarchical resonant modes.

the unit cell, while mode B demonstrates out-of-plane motion. Mode C resembles mode A, with corner-localized vibrations, whereas mode D is analogous to mode B but involves all four single elements vibrating simultaneously. This collective motion results in a larger effective inertia than mode B of the non-hierarchical element, thereby causing a downward shift in the resonant frequency. In essence, the hierarchical design modifies the mass-to-stiffness ratio and introduces new localized resonant modes, both of which promote the formation of new band gaps and reduce their corresponding frequencies.

To further assess the wave suppression performance of the proposed SMs, transmittance is calculated as the ratio of the output to the input, defined as the magnitude ratio of the response displacement W_{out} to the excitation displacement W_{in}:

$$\tau = 20\log_{10}(|W_{\text{out}} / W_{\text{in}}|). \tag{10}$$

Fig. 5(a) depicts the input and output lines on the layout of SMs composed of 10 × 6 unit cells, with wave excitation propagating along the *x*-direction. Perfectly matched layers (PML) are applied on the edges to absorb outgoing waves and emulate an infinite medium. Theoretically, a band gap is defined as the frequency range where the transmittance falls below 0 dB. However, relying solely on this criterion can be misleading, as sudden impedance mismatches at the interface between the soil and SMs may induce partial wave reflections, even outside band gaps, thereby reducing transmittance amplitude [77].

For reference, the main attenuative region identified from the band structure in Fig. 2 is shaded in Fig. 5(b), which depicts the transmittance curves of the proposed SMs. Since each hierarchical SM unit cell comprises four single unit cells, the transmittance of the NPR-based SM is evaluated for both 10 × 6 and 20 × 12 configurations. Although the transmittance occasionally falls below 0 dB outside the predicted band gaps, the main attenuative regions closely align with the valleys in the transmittance curves for both the NPR-based non-hierarchical and hierarchical SMs. By contrast, the rubber-based hierarchical SM shows poor alignment between its transmittance curve and the expected attenuation region, which can be attributed to the larger number of propagating modes between band gaps, as discussed in Fig. 2.

Moreover, due to the *x*-directional excitation, directional band gaps also contribute to the transmittance valleys, notably between 3-8 Hz in Fig. 5(b). Overall, the NPR-based hierarchical SM exhibits lower transmittance than both the rubber-based hierarchical and the NPR-based SMs, along with a greater number of attenuation regions, clearly demonstrating its superior vibration suppression performance.

3. Wave suppression for surface wave

In addition to Lamb waves studied in the previous section, surface waves represent another critical type of seismic waves propagating in a half-space medium and are often the primary cause of severe structural damage. This section evaluates the wave suppression efficiency of the NPR-based hierarchical SM with the negative effective mass effect. Both frequency-domain and time-domain analyses are conducted, with particular emphasis on the practical implications for a steel frame structure.

3.1. Model and methods

The concept of negative effective mass effect was first introduced in the context of an infinite lattice system [78], and was later demonstrated by Wang et al. [29] in SMs using a simplified mass-spring lattice model. According to Newton's second law, the equilibrium equation for the *n*th unit cell can be expressed as:

$$K(u_{n-1} - u_n) - K(u_n - u_{n+1}) - Gu_n = -m\omega^2 u_n, \tag{11}$$

where K and G denote the spring stiffness in horizontal and vertical directions, respectively. Additionally, substituting Eq. (2) into Eq. (11) yields:

$$m\omega^2 - G = 4K\sin^2\frac{qa}{2}. \tag{12}$$

Thus, the effective mass can be expressed as:

$$m_{eff} = m - \frac{G}{\omega^2} = m\left(1 - \frac{\omega_0^2}{\omega^2}\right), \tag{13}$$

with a cut-off frequency of $\omega_0 = \sqrt{G/m}$. Based on Eq. (13), we propose an NPR-based hierarchical SM with a square section embedded in soil. This design enhances stiffness G while maintaining the mass m, thereby achieving the negative effective mass effect. Fig. 6(b) illustrates the configuration of the proposed SM for surface wave attenuation, while Fig. 6(c) presents a comparable SM without the square section for later comparison. Since surface waves propagate in a half-space, a soil substrate with a thickness of 10L is placed beneath the SMs, which is sufficiently large relative to the wavelength of interest [79], and a steel-made square section is incorporated with a thickness of $t_c = L_a - L_b$, as shown in Fig. 6(a). The height of the steel section is set to 5L to ensure an effective enhancement of stiffness G. Fixed boundary conditions are applied at the bottom of the unit cells, and Bloch's periodic boundary conditions are imposed on the lateral sides, as illustrated in Fig. 6. The other geometric and material parameters are the same as those in Fig. 1.

Furthermore, the sound cone method [80] is utilized to distinguish surface wave modes from body wave modes in the band structure. Specifically, surface wave modes lie within the sound cone, whereas body wave modes appear outside it. The sound cone curve is defined as:

$$f = \frac{kc_{soil}^s}{2\pi}, \tag{14}$$

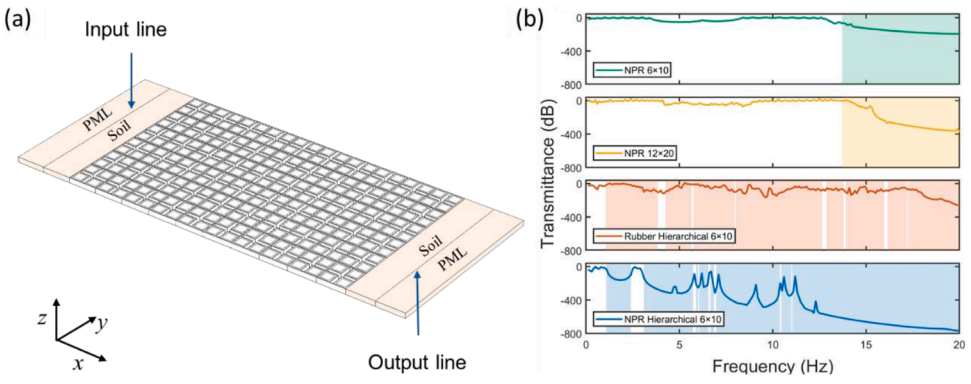

Fig. 5. Frequency-domain analysis of SMs. (a) SM layout containing 10 × 6 unit cells with PML boundaries; waves propagate along the x-direction. (b) Transmittance curves of four SM configurations, with shaded regions indicating band gaps identified from the band structure analysis.

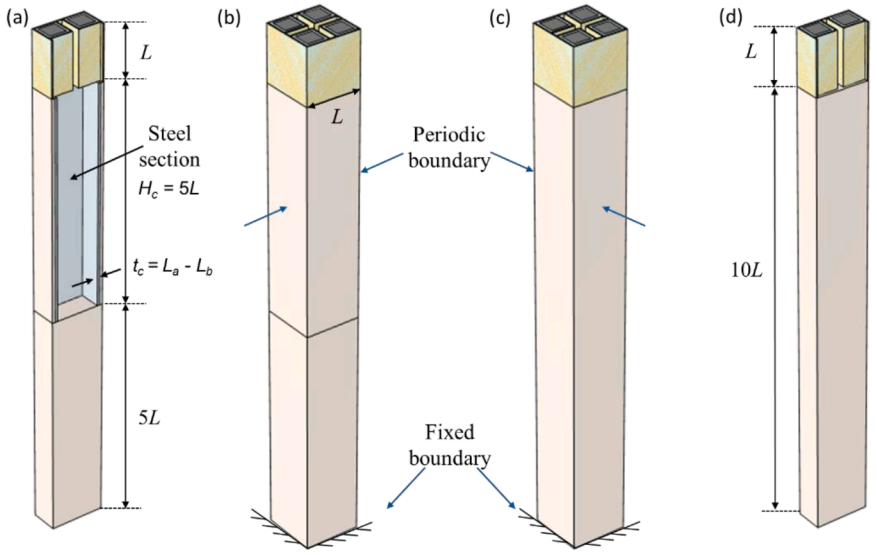

Fig. 6. Schematics of proposed SMs for surface wave suppression: (a) cross-sectional view of (b) an NPR-based hierarchical unit cell with a square section; (c) an NPR-based hierarchical unit cell; and (d) cross-sectional view of (c).

where $k = \sqrt{k_x^2 + k_y^2}$, shear wave velocity in the soil $c_{soil}^s = \sqrt{\frac{E_{soil}}{2(1+\upsilon_{soil})\rho_{soil}}}$.

3.2. Frequency domain validation

Fig. 7 presents the band structures of the proposed SMs, with the sound cone plotted in red. The region outside the sound cone is shaded in light red, while full band gaps are highlighted in blue. Consistent with the SMs designed for Lamb wave suppression discussed in earlier sections, the NPR-based hierarchical SM shifts the operational frequency range of the non-hierarchical SM toward lower frequencies. Compared to the NPR-based SM, the hierarchical design shown in Fig. 7(b) exhibits more full band gaps, spanning the frequency ranges of [0, 2.22] Hz, [6.99, 7.37] Hz, [10.01, 10.08] Hz, and [26.04, 28.15] Hz. It is worth noting that a band gap in the frequency range of 19.70–21.79 Hz is observed in Fig. 7(a) but appears to vanish in the hierarchical SM. Its apparent disappearance arises from the emergence of a deaf dispersion branch in Fig. 7(b), which obscures the visual identification of the band gap, even though the band gap still exists. This phenomenon is further examined and clarified in the subsequent transmittance analysis.

For comparison, the band structure of the rubber-based hierarchical SM is plotted in Fig. 7(c). Although it generates multiple band gaps, this configuration also allows more surface wave modes between the attenuation zones than the NPR-based design. In contrast, the hierarchical SM with a square section, as shown in Fig. 7(d), exhibits a continuous and complete band gap, entirely free of surface wave modes within the sound cone. Therefore, the term ultra-wide SM is used hereafter to refer to this configuration for brevity. The vibration modes corresponding to four representative points in Fig. 7(d) are illustrated in Fig. 8. At points B and C, it can be noted that wave energy is primarily concentrated in the half-space, whereas at points A and D, vibrations are predominantly confined near the surface. This difference in vibration patterns suggests a gradual attenuation of vibration as it propagates from the surface into the underlying soil.

Fig. 9 shows the schematic diagram of the SM configuration used for frequency- and time-domain simulations, consisting of 30 unit cells. PMLs with a thickness of 3*L* are applied to the bottom and lateral boundaries, while periodic boundary conditions are imposed in the out-of-plane direction. It is important to note that for the time-domain analysis, low reflection boundary conditions are used in place of PMLs

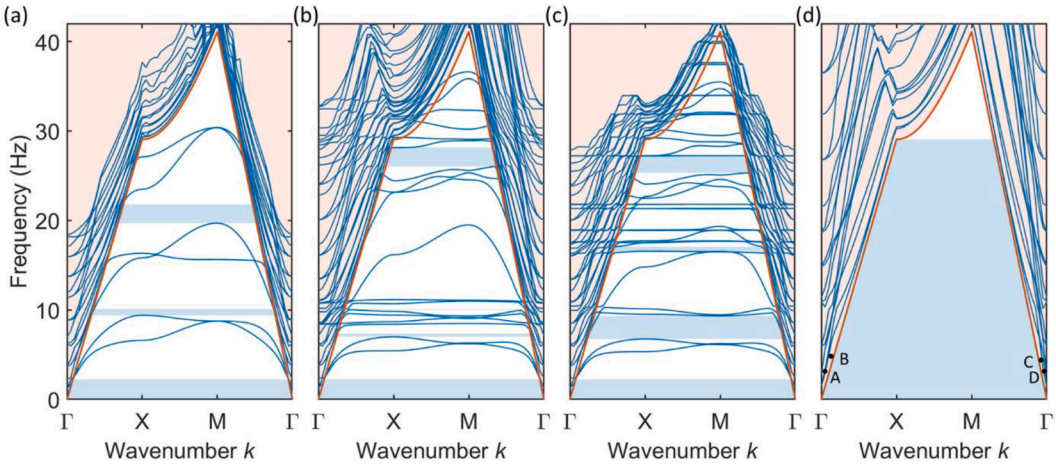

Fig. 7. Band structures of proposed SMs. The sound cone is shown in red, with the region outside shaded light red, and full band gaps highlighted in blue. (a) NPR-based SM, (b) NPR-based hierarchical SM, (c) rubber-based hierarchical SM, and (d) NPR-based hierarchical SM with a square section (ultra-wide SM), demonstrating enhanced low-frequency vibration suppression and broader full band gaps.

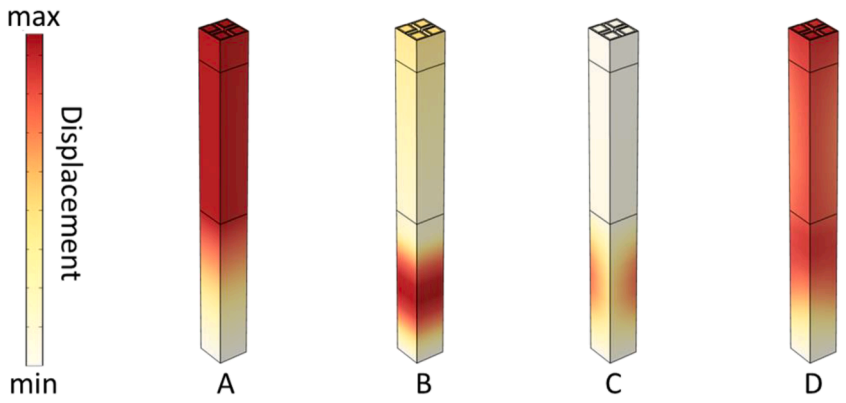

Fig. 8. Typical vibration modes of ultra-wide SM at four points marked in Fig. 7(b).

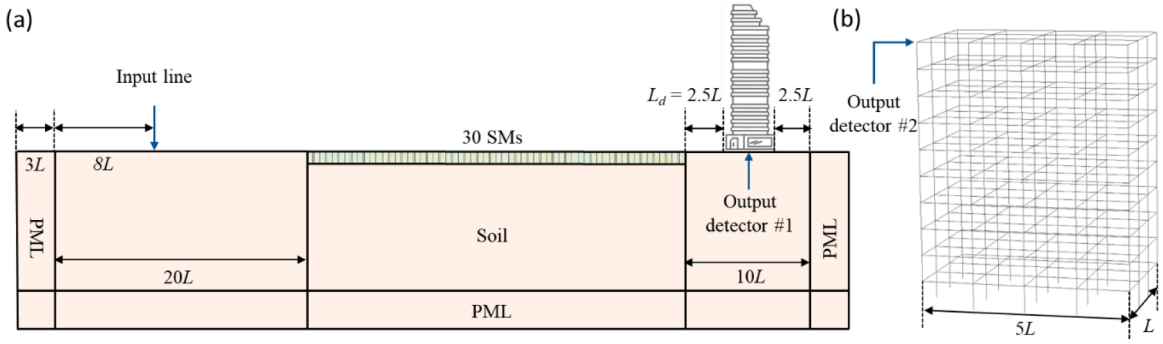

Fig. 9. Schematic of the SM system for frequency- and time-domain analyses. (a) Finite-length SM with 30 unit cells, PMLs applied at the bottom and lateral boundaries. (b) Steel frame structure with output detector #1 at the bottom and output detector #2 at the top.

[71]. The excitation is applied at the input line, located 12L away from the SMs, to ensure that only surface waves reach the SM system. Two output detectors are placed: one on the right side of the domain, as shown in Fig. 9(a), and the other at the top of the steel frame structure, as shown in Fig. 9(b). It should be noted that detector #1 provides the primary and objective evaluation of the SM's wave mitigation performance, as it directly reflects wave attenuation independent of any structural configuration, whereas detector #2 serves only as a reference case to illustrate the potential reduction in structural response for a representative building configuration. The transmittance τ_s of the proposed SMs is defined by the amplitude reduction factor A_r, based on the average displacement U within the area S of detector #1:

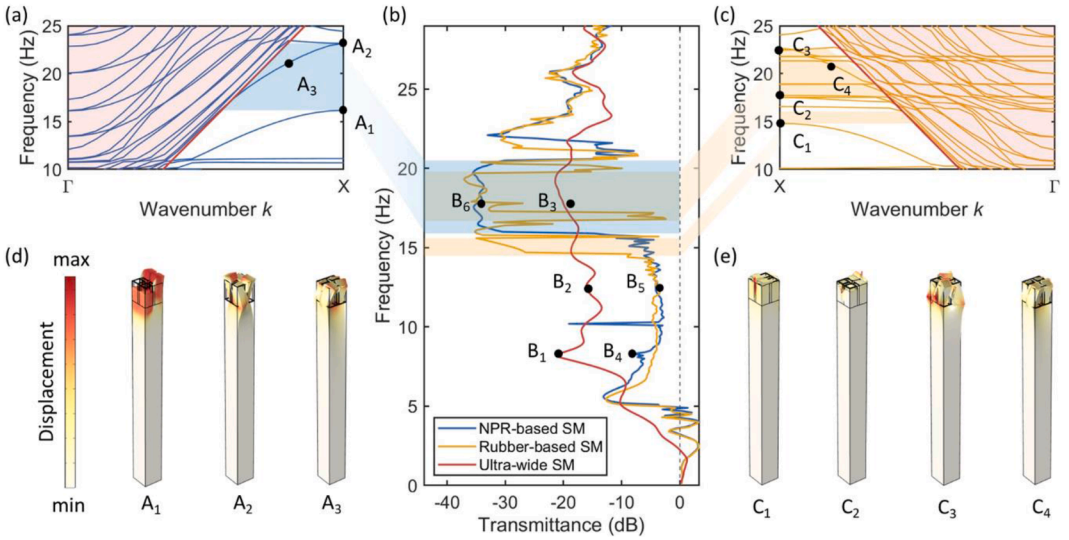

Fig. 10. Frequency-domain analysis of proposed SMs. (a) Band structure of the NPR-based hierarchical SM along the Γ–X path, highlighting the directional band gap. (b) Transmittance curves of the three SMs below 29 Hz. (c) Band structure of the rubber-based hierarchical SM along the Γ–X path, showing discontinuous directional band gaps. (d) Vibration modes at the upper and lower edges of the directional band gap for the NPR-based hierarchical SM. (e) Corresponding vibration modes at the upper and lower edges of the directional band gap for the rubber-based hierarchical SM.

$$A_r = \frac{U_{\text{with}}}{U_{\text{without}}}, \tag{15}$$

$$\tau_s = 20 * \log_{10}\left(\frac{1}{S}\int_0^S A_r dx\right). \tag{16}$$

Furthermore, when the vibration energy spreads over a wide spectrum, another essential criterion for evaluating the effectiveness of vibration suppression is the average transmittance τ_{avg} [16], defined as:

$$\tau_{avg} = \frac{1}{\omega_B - \omega_A}\int_{\omega_A}^{\omega_B} \tau(\omega)d\omega = \frac{1}{\omega_B - \omega_A}\sum_{i=1}^{M}[\tau(\omega_A + i\Delta\omega)\Delta\omega], \tag{17}$$

where $M = (\omega_B - \omega_A)/\Delta\omega$. $\Delta\omega$ is the sampling frequency interval over the specified frequency range [ω_A, ω_B]. A smaller average transmission τ_{avg} signifies a stronger vibration suppression ability.

Fig. 10 presents the transmittance curves of the proposed SMs below 29 Hz, corresponding to the upper frequency limit of the attenuation zone defined by the sound cone curve. For reference, the band structures along the Γ–X path are shown in Fig. 10(a) and (c), where directional band gaps are clearly identified. Although no full band gaps can be observed in Fig. 7(b) or (c) within the 15-20 Hz range, multiple dispersion branches along the Γ–X path give rise to the directional band gap, as highlighted in Fig. 10(a) and (c). Fig. 10(d) and (e) display the vibration modes at the upper and lower edges of these directional band gaps. The horizontal resonance is found at A_3 and C_4, which cannot suppress the surface wave, suggesting this dispersion curve is deaf. Vertical resonance is evident across other cases, indicating strong coupling with surface waves. At the upper boundary frequencies (A_2 and C_3), local bending and torsional modes dominate the unit cell response. In contrast, the lower boundary frequencies (A_1, C_1, and C_2) are characterized by more pronounced vertical vibration modes. It is worth noting that the band gaps observed in the transmittance curve shift slightly toward lower frequencies compared to those in the band structures. This discrepancy is primarily attributed to the assumption of infinite periodicity in band structure computations, a condition that cannot be fully realized in transmittance simulations.

The τ_{avg} values for the NPR-based hierarchical, the rubber-based hierarchical, and the ultra-wide SMs are calculated to be -13.18 dB, -13.60 dB, and -14.27 dB, respectively. Although the rubber-based hierarchical SM exhibits a slightly lower τ_{avg} than the NPR-based hierarchical SM, its attenuation zones are less continuous, as shown in Fig. 10 (b). This discontinuity is attributed to the presence of additional branches within the sound cone in Fig. 10(c). While both NPR-based and rubber-based hierarchical SMs show strong attenuation in the 15-20 Hz range, the ultra-wide SM demonstrates superior vibration suppression performance in the lower frequency range of 5–15 Hz. Furthermore, its lower τ_{avg} across the frequency range of interest confirms the effectiveness of the band gap induced by the negative effective mass mechanism in achieving broadband vibration suppression.

The displacement fields at three representative frequencies marked in Fig. 10(b), 8.1 Hz (B1 and B4), 12.4 Hz (B2 and B5), and 18.6 Hz (B3 and B6), are presented in Fig. 11. At 8.1 Hz, both the ultra-wide SM and the NPR-based hierarchical SM exhibit transmittance values below 0 dB; however, they attenuate vibrations through different mechanisms in the low-frequency domain. In B_1 of Fig. 11(a), vibrations primarily propagate into the half-space, while in B_4 of Fig. 11(b), significant vibrations are concentrated within the SM structure. Furthermore, in B_5 of Fig. 11 (b), the wave traverses the SM array while inducing substantial internal vibrations within the unit cells, suggesting that the NPR-based hierarchical SM attenuates vibration through internal resonance and energy dissipation. In contrast, at a higher frequency in B_6 of Fig. 11(b), surface waves deflect upon interacting with the SMs and convert into body waves propagating at approximately a 45-degree angle into the soil. A similar wave transformation is observed at lower frequencies in B_1, B_2, and B_3 of Fig. 11(a), indicating that the ultra-wide SM attenuates seismic waves by redirecting the propagation path and dispersing energy into a more compliant medium, such as the surrounding soil. This behavior suggests that within the band gap induced by the negative effective mass mechanism, wave propagation is inhibited, causing the waves to become evanescent and either reflected or rapidly attenuated.

3.3. Time domain validation

While the preceding sections demonstrated the wave attenuation performance of the proposed SMs under harmonic excitation, real earthquakes are inherently non-harmonic. Therefore, time-domain validation is conducted using real seismic records, as illustrated in the layout of Fig. 9. Two representative earthquake signals, El Centro and Taft, obtained from the PEER Ground Motion Database, are employed as input excitations. To evaluate the effectiveness of seismic protection for structures, a 10-story steel frame building with a length of 5L and a width of L is positioned above output detector #1, as shown in Fig. 9(b).

Fig. 12 presents the seismic wave attenuation results for detector #1 (ground level) in both the time domain and the corresponding Fourier spectra for the El Centro and Taft earthquake records. As the most intense vibration occurs within the first 30 seconds of both records, only this portion is considered in our analysis. As shown in Fig. 12(a) and (b), the ultra-wide SM demonstrates significant effectiveness in acceleration suppression in the time domain for both seismic records. In the frequency domain, the amplitude response of the model incorporating the ultra-wide SM notably decreases beyond 2.6 Hz, which corresponds to the frequency at which transmittance drops below 0 dB in Fig. 11(b). Furthermore, while the NPR-based hierarchical SM demonstrates slightly lower suppression efficiency in the time domain, it outperforms the ultra-wide SM in attenuating spectral amplitudes within the 15–20 Hz range in the Fourier spectra of Fig. 12(a) and (b), consistent with the results from the frequency-domain analysis.

To further evaluate the seismic protection provided to the building

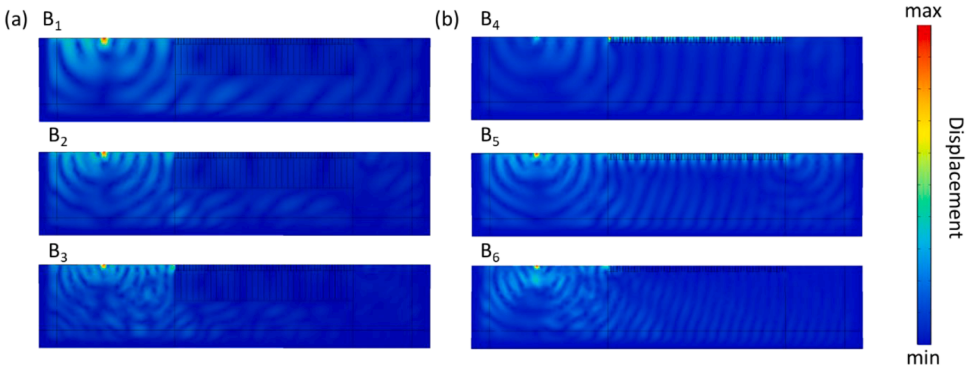

Fig. 11. Displacement fields at three representative frequencies (8.1 Hz, 12.4 Hz, and 18.6 Hz) for the two SM configurations, illustrating surface wave redirection and body wave conversion: (a) ultra-wide SMs and (b) NPR-based hierarchical SMs.

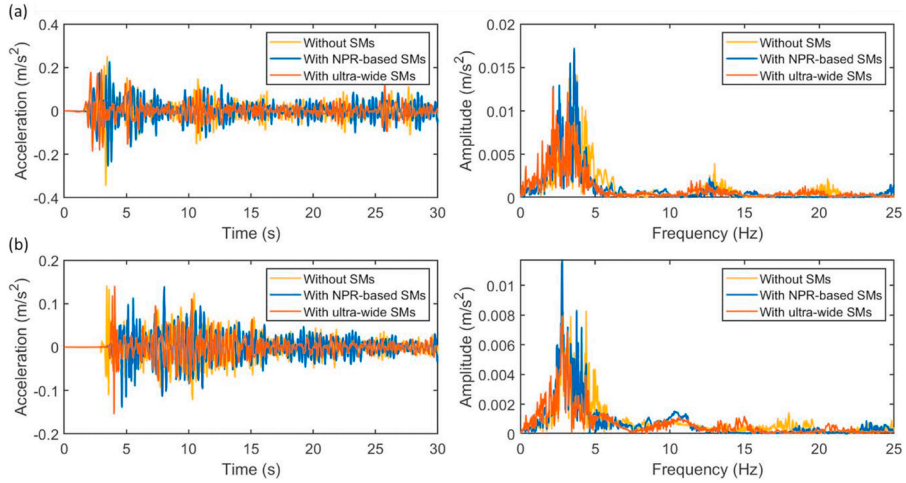

Fig. 12. Seismic wave attenuation at detector #1 (ground level) achieved by proposed SMs illustrated in the time domain and corresponding Fourier spectra, for earthquake excitations from (a) El Centro record and (b) Taft record.

by the proposed SMs, detector #2 is positioned at the top of the building, as shown in Fig. 9(b). The corresponding acceleration responses and their Fourier spectra are presented in Fig. 13. Both the NPR-based hierarchical SM and the ultra-wide SM exhibit significant reductions in acceleration, validating their effectiveness in vibration suppression. To quantitatively assess this performance, a reduction ratio is defined as $a = \left(\mathrm{RMS}^{\mathrm{Without}} - \mathrm{RMS}^{\mathrm{With}}\right)/\mathrm{RMS}^{\mathrm{Without}} \times 100\%$, where RMS denotes the root-mean-square acceleration at the top of the building. It is worth mentioning that the upper floors undergo significantly larger sway than the base, and the acceleration measured at detector #2 naturally exceeds that at detector #1. The NPR-based hierarchical SM demonstrates greater reduction effectiveness under the El Centro record than under the Taft record. For both El Centro and Taft seismic waves, the building protected by the ultra-wide SM achieves higher reduction ratios (90.93% and 84.12%) than the NPR-based hierarchical SMs (84.60% and 75.60%). These results further demonstrate that the negative effective mass effect enhances seismic protection in practical structural applications.

3.4. Parametric study

Based on the previous analysis, the influences of section height and the location of the protected building are investigated in detail. Unless otherwise specified, the default geometric and material parameters are the same as those listed in Table 1.

3.4.1. Influence of steel section height

As discussed in earlier sections, the steel section shown in Fig. 6 enhances stiffness and thus promotes the realization of the negative effective mass effect. However, as shown in Figs. 10(b) and 12, the proposed SMs do not exhibit pronounced attenuation in the 0-5 Hz range. To address this limitation, the section height becomes a critical factor governing the onset frequency of effective suppression. Fig. 14 depicts the evolution of band structures and transmittance curves as the normalized section height H_x ($H_x = H_c/L$) varies from 0.5 to 10. When $H_x = 0.5$, the NPR effect and the negative effective mass mechanism act synergistically to produce a wider first band gap (0–2.8 Hz) compared with the configuration without the steel section, as well as a broader second band gap. Surface wave modes remain within the sound cone for $H_x = 1$. In this case, besides the band gap below 24 Hz, a directional band gap also contributes to the attenuation zone between 25 and 29 Hz, as indicated by the light-blue shading in the transmittance plot. As the section height, and thus stiffness, increases, the wave modes gradually shift toward higher frequencies. As illustrated in Fig. 14(a), increasing the section height causes surface-wave modes to gradually shift upward in frequency, merge with body-wave branches, and eventually vanish within the sound cone. This behavior corresponds to the frequency

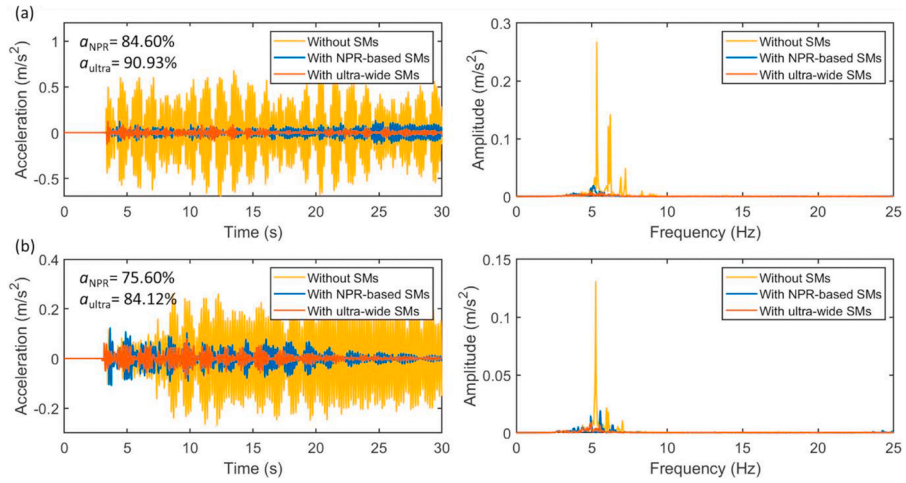

Fig. 13. Acceleration responses at detector #2 (top of the structure) in the time domain and corresponding Fourier spectra, based on (a) El Centro and (b) Taft seismic records. Ultra-wide SM achieves higher reduction ratios (90.93% and 84.12%) than NPR-based hierarchical SM (84.60% and 75.60%), demonstrating superior seismic protection performance.

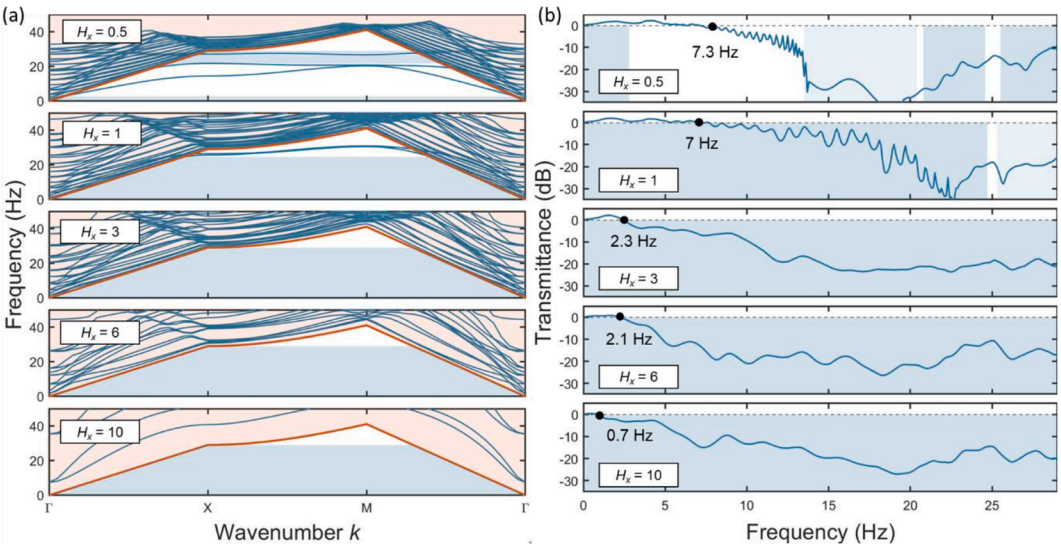

Fig. 14. Influence of normalized section height $H_x = H_c/L$ on seismic attenuation performance: (a) band structures showing upward shifts and eventual disappearance of surface wave modes within the sound cone as stiffness increases, and (b) corresponding transmittance curves illustrating enhanced low-frequency suppression.

interval in which the negative effective mass mechanism dominates, thereby extending the upper bound of the associated band gap from 24 to 29 Hz. Correspondingly, the wave suppression capacity improves with section height, as reflected by τ_{avg} values of -10.18 dB, -15.26 dB, -15.73 dB, and -15.62 dB across the last four scenarios. Moreover, in the ultra-low frequency range, the wave suppression performance becomes more pronounced, as shown in Fig. 14(b). Specifically, the onset frequency at which the transmittance falls below 0 dB shifts toward 0 Hz, indicating enhanced attenuation capability.

3.4.2. *Influence of spatial placement*

Fig. 15 illustrates the influence of the normalized distance L_x between the SM system and the protected steel frame structure on the transmittance curves and reduction ratio under the El Centro and Taft seismic records. The normalized distance L_x is defined as $L_x = L_d/L$, where L_d denotes the actual spatial distance between the SM system and the building, as shown in Fig. 9. When the structure is positioned close to the SM system, low-frequency suppression is enhanced, as evidenced by lower transmittance values in Fig. 15(a). By contrast, for frequencies above 10 Hz, suppression is more effective when the building is located farther from the SM system. Fig. 15(b) shows the corresponding variation in RMS acceleration and its reduction ratio at the building top. Despite minor fluctuations, the overall trend indicates that smaller L_x values yield lower RMS acceleration and higher reduction ratios, confirming that closer SM placement enhances seismic protection under both earthquake records. These observations suggest that the optimal placement of SMs depends on the dominant frequency content of the input seismic wave. In particular, shorter distances are more effective for mitigating low-frequency vibrations, while longer distances allow high-frequency components to dissipate more efficiently before reaching the structure.

3.5. *Experimental validation*

To further validate the theoretical predictions, a laboratory-scale prototype consisting of 5 × 2 unit cells was fabricated using 3D printing and subsequently coated with rubber sheets. Polylactic Acid (PLA) was chosen as the printing material owing to its ease of processing and cost-effectiveness. Since the influence of NPR materials on the performance of the seismic metamaterial has already been experimentally demonstrated [71], the present experiment focuses on validating the two additional mechanisms considered in this work: (i) the negative effective mass effect, examined through comparisons between ultra-wide and rubber-based SMs, and (ii) the role of hierarchical topology, assessed by comparing single-element and hierarchical SM configurations. For compatibility with the laboratory environment, the

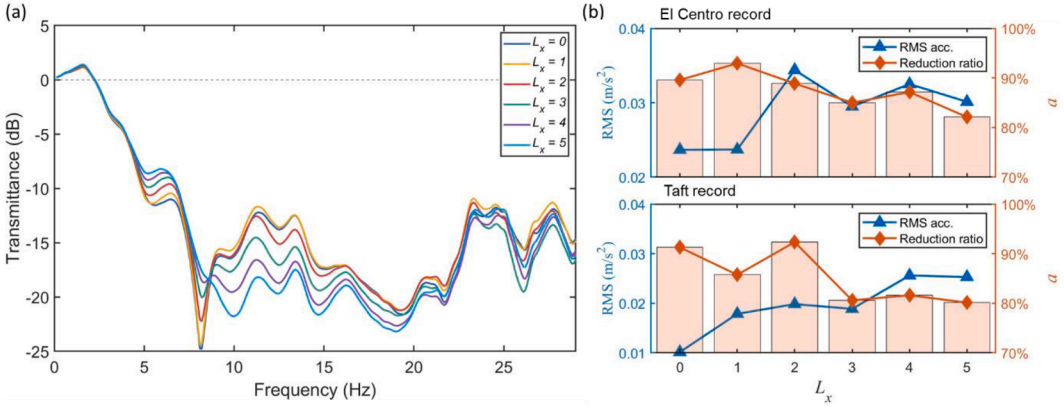

Fig. 15. Influence of normalized distance $L_x = L_d/L$ between SM system and protected steel frame structure on seismic attenuation performance: (a) transmittance curves showing enhanced low-frequency suppression at smaller L_x, (b) corresponding RMS acceleration and reduction ratio under El Centro and Taft seismic records.

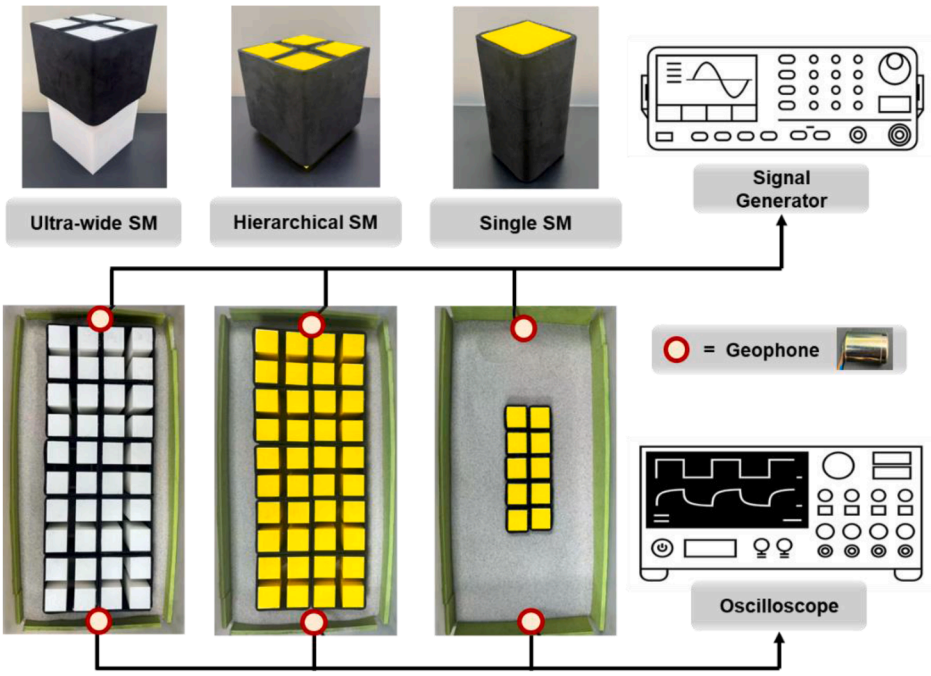

Fig. 16. Experimental setup for vibration testing of ultra-wide, hierarchical, and single SM prototypes. Excitations are applied at the top by a signal generator, while responses are measured by a geophone at the bottom and recorded with an oscilloscope.

prototype dimensions were set as follows: $L = 0.1125$ m, $L_a = 0.05$ m, $L_b = 0.045$ m, $t = 0.1125$ m, and $H_c = 0.1125$ m.

The experimental setup is shown in Fig. 16. A broadband excitation covering 5-250 Hz was generated using a signal generator (Rigol DG1022). A pair of geophones (GDH-4.5) was used to induce and detect vibrations, with the signals recorded by an oscilloscope (Tektronix MSO44). The soil container, measuring 73 × 30 × 40 cm^3, was filled with Ottawa 2030 sand to a depth of 30 cm. Its inner surfaces were lined with acoustic panels to minimize wave reflections. Ultra-wide SMs (white) and rubber-based SMs (yellow) were fabricated via 3D printing.

The transmittance curves, calculated using Eq. (16), are presented in Fig. 17(b). When compared with the FEM predictions (the upper panel of Fig. 17(b)), the experimental results show good overall agreement, although the measured transmittance values are generally lower. This discrepancy is primarily attributed to the pore spaces in the moist sand layers. As shown in Fig. 16, the container width slightly expands due to sand settlement, making it difficult to achieve perfect compaction. Consequently, greater energy dissipation occurred in the experiment, resulting in lower output responses and thus reduced transmittance compared with FEM simulations.

Despite these differences, the experimental results in the lower panel of Fig. 17(b) clearly demonstrate the enhanced vibration suppression achieved by the ultra-wide SM compared with the rubber-based SM, and the superior performance of the hierarchical configuration relative to the single-element design. The single-element SM exhibits the weakest vibration suppression performance, as the tested frequency range lies outside its band gap. The ultra-wide SM consistently achieves deeper attenuation across a broader frequency range, whereas the rubber-based SM provides moderate suppression with narrower attenuation regions. Fig. 17(a) and (c) further demonstrate the effectiveness of vibration

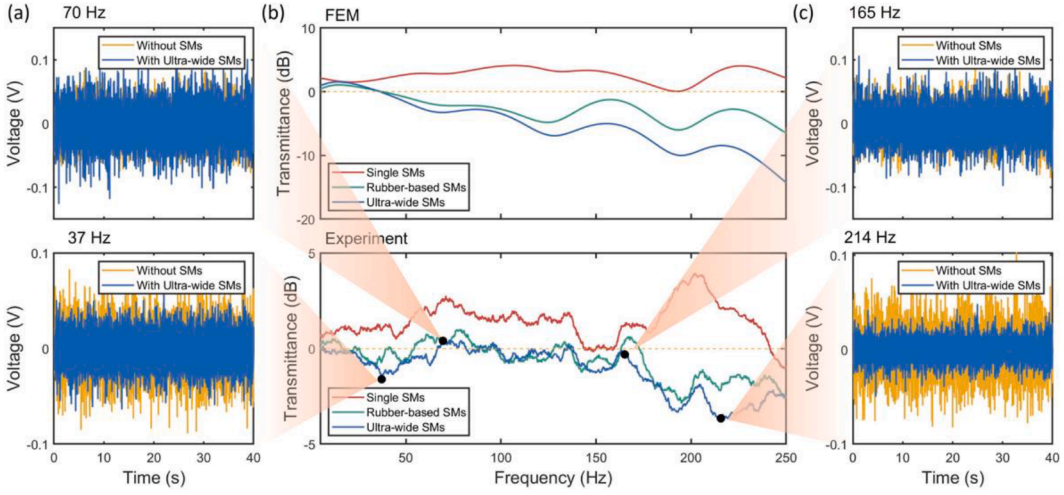

Fig. 17. Experimental validation for wave attenuation. (a) Measured output voltage at representative frequency points: peak (70 Hz) and valley (37 Hz). (b) Transmittance curves obtained from FEM simulations and experiments for single, rubber-based, and ultra-wide SMs, showing ultra-wide SM achieves superior wave suppression. (c) Measured output voltage at representative frequency points: peak (165 Hz) and valley (214 Hz).

suppression by comparing output signals with and without SMs at the representative peak and valley frequencies. The ultra-wide SM produces a pronounced reduction in vibration amplitude, validating its strong potential for practical seismic wave attenuation.

4. Conclusions

This paper presents hierarchical seismic metamaterial (SM) designs incorporating auxetic foams with negative Poisson's ratio for ultra-low-frequency and broadband seismic wave attenuation. For Lamb wave suppression, the $k(\omega)$ technique and finite element method are employed. The resulting complex band structures reveal the presence of evanescent modes, a downward shift in band gap frequencies, and additional band gaps induced by multi-scale hierarchical resonances. These features are verified by frequency-domain transmittance simulations, which demonstrate consistent attenuation across multiple frequency regions.

To mitigate surface waves, the SM configuration is designed by embedding a square section into the NPR-based hierarchical unit cell. This design induces a negative effective mass effect, resulting in continuous and wide band gaps, entirely free of surface wave modes within the sound cone. In the proposed design, low-frequency wave suppression is primarily governed by the negative effective mass effect associated with section height and stiffness, while the hierarchical topology and NPR behavior play a critical role in enhancing attenuation continuity and suppressing unwanted propagating modes. As a result, broadband and robust seismic wave mitigation is achieved through the combined contributions of these complementary mechanisms. Frequency- and time-domain analyses confirm the effectiveness of this ultra-wide SM in redirecting surface waves and converting them into body waves, which dissipate energy into the surrounding soil. The practical efficacy of the SM design is evaluated using real seismic input records (El Centro and Taft) and a 10-story steel frame building situated downstream of the seismic source, with the SMs embedded in the intervening soil. Results show significant reductions in RMS acceleration at the top floor, 90.93% and 84.12%, respectively, demonstrating the effectiveness of the SMs in mitigating seismic impact. Furthermore, a comprehensive parametric study identifies the key factors influencing suppression performance, revealing that both geometric configuration and spatial placement of SMs are critical for optimizing seismic protection. Finally, a laboratory-scale experiment is conducted to validate the promising vibration suppression efficiency of the ultra-wide SM.

Overall, the hierarchical NPR-based SM design is assessed for both Lamb and surface wave attenuation, providing a scalable and effective strategy to enhance the seismic resilience of critical infrastructure.

CRediT authorship contribution statement

Jiazhen Zhang: Writing – original draft, Validation, Software, Methodology, Investigation, Data curation. **Chaoyang Zhao:** Investigation. **Guobiao Hu:** Writing – review & editing, Supervision, Conceptualization. **Dewen Yu:** Methodology. **Xingbo Pu:** Methodology. **Yaowen Yang:** Writing – review & editing, Supervision, Conceptualization.

Declaration of competing interest

The authors declare that they have no known competing financial interests or personal relationships that could have appeared to influence the work reported in this paper.

Acknowledgments

This work was financially supported by the State Key Laboratory of Structural Analysis for Industrial Equipment, Dalian University of Technology, China (S22311), the National Natural Science Foundation of China (Grant No. 52305135), and the Guangzhou Municipal Science and Technology Bureau (Grant Nos. SL2023A03J00869, SL2023A04J01741).

Data availability

Data will be made available on request.

References

[1] Sigalas MM, Economou EN. Elastic and acoustic wave band structure. J. Sound. Vib. 1992;158:377–82.
[2] Kushwaha MS, Halevi P, Martínez G, Dobrzynski L, Djafari-Rouhani B. Theory of acoustic band structure of periodic elastic composites. Phys. Rev. B 1994;49:2313–22.
[3] Sánchez-Pérez JV, Caballero D, Mártinez-Sala R, Rubio C, Sánchez-Dehesa J, Meseguer F, Llinares J, Gálvez F. Sound attenuation by a two-dimensional array of rigid cylinders. Phys. Rev. Lett. 1998;80:5325–8.
[4] Kafesaki M, Sigalas MM, García N. Frequency modulation in the transmittivity of wave guides in elastic-wave band-gap materials. Phys. Rev. Lett. 2000;85:4044–7.
[5] Colombi A, Colquitt D, Roux P, Guenneau S, Craster RV. A seismic metamaterial: the resonant metawedge. Sci. Rep. 2016;6:27717.
[6] Brûlé S, Javelaud EH, Enoch S, Guenneau S. Experiments on seismic metamaterials: molding surface waves. Phys. Rev. Lett. 2014;112:133901.
[7] Aravantinos-Zafiris N, Sigalas M. Large scale phononic metamaterials for seismic isolation. J. Appl. Phys. 2015;118.
[8] Khlopotin A, Olsson P, Larsson F. Transformational cloaking from seismic surface waves by micropolar metamaterials with finite couple stiffness. Wave Motion. 2015;58:53–67.
[9] Fur L-S, Yang HTY, Ankireddi S. Vibration control of tall buildings under seismic and wind loads. J. Struct. Eng. 1996;122:948–57.
[10] Symans MD, Charney FA, Whittaker A, Constantinou MC, Kircher C, Johnson MW, McNamara RJ. Energy dissipation systems for seismic applications: current practice and recent developments. J. Struct. Eng. 2008;134:3–21.
[11] Xiong C, Liu Y, Xie L, Li Q. Seismic performance control of tall buildings using a novel self-centering shear wall system. Int. J. Struct. Stabil. Dyn. 2022;22:2250131.
[12] Chang K-C, Lin Y-Y. Seismic response of full-scale structure with added viscoelastic dampers. J. Struct. Eng. 2004;130:600–8.
[13] Achaoui Y, Ungureanu B, Enoch S, Brûlé S, Guenneau S. Seismic waves damping with arrays of inertial resonators. Extreme Mech. Lett. 2016;8:30–7.
[14] Krödel S, Thomé N, Daraio C. Wide band-gap seismic metastructures. Extreme Mech. Lett. 2015;4:111–7.
[15] Xu Y, Xu R, Peng P, Yang H, Zeng Y, Du Q. Broadband H-shaped seismic metamaterial with a rubber coating. Europhys. Lett. 2019;127:17002.
[16] Zhang J, Peng X, Yu D, Hu G, Yang Y. Rigid-elastic combined metamaterial beam with tunable band gaps for broadband vibration suppression. J. Vib. Acoust. 2024;146.
[17] Meseguer F, Holgado M, Caballero D, Benaches N, Sánchez-Dehesa J, López C, Llinares J. Rayleigh-wave attenuation by a semi-infinite two-dimensional elastic-band-gap crystal. Phys. Rev. B 1999;59:12169–72.
[18] Geng Q, Zhu S, Chong KP. Issues in design of one-dimensional metamaterials for seismic protection. Soil Dyn. Earthq. Eng. 2018;107:264–78.
[19] Jia Q, Zhang J, Han D, Wen J, Yu D. Bragg scattering-driven anisotropic metabeam with multi-scale architecture for ultra-broadband vibration suppression at high structural stiffness. Eng. Struct. 2025;336:120493.
[20] Qiu Y, Li J, Song Z. A novel active switchable multi-channel waveguide based on the Bragg scattering mechanism and the force-magnetic coupling effect. Multidiscipl. Model. Mater. Struct. 2025;21:619–32.
[21] Eyring CF. Jungle acoustics. J. Acoust. Soc. Am. 1946;18:257–70.
[22] Liu Y-f, Huang J-k, Li Y-g, Shi Z-f. Trees as large-scale natural metamaterials for low-frequency vibration reduction. Constr. Build. Mater. 2019;199:737–45.
[23] Colombi A, Roux P, Guenneau S, Gueguen P, Craster RV. Forests as a natural seismic metamaterial: Rayleigh wave bandgaps induced by local resonances. Sci. Rep. 2016;6:19238.
[24] Muhammad TWu, Lim C. Forest trees as naturally available seismic metamaterials: low frequency Rayleigh wave with extremely wide bandgaps. Int. J. Struct. Stabil. Dyn. 2020;20:2043014.
[25] Zhang K, Luo J, Hong F, Deng Z. Seismic metamaterials with cross-like and square steel sections for low-frequency wide band gaps. Eng. Struct. 2021;232:111870.
[26] Muhammad, Lim CW, Reddy JN. Built-up structural steel sections as seismic metamaterials for surface wave attenuation with low frequency wide bandgap in layered soil medium. Eng. Struct. 2019;188:440–51.
[27] Gao L, Cai C, Ming Mak C, He X, Zou Y, Wu D. Surface wave attenuation by periodic hollow steel trenches with Bragg band gap and local resonance band gap. Constr. Build. Mater. 2022;356:129289.
[28] Wang W, Wei G, Yifan D, Zhou Y. Attenuation analysis of low-frequency surface waves in the ultra-low-frequency bandgap of embedded seismic metamaterials. Mech. Adv. Mater. Struct. 2024;31:6863–73.
[29] Wang Z, Shen Y, Tan J, Yang H, Peng P, Liu F, Du Q. A broadband zero-frequency seismic metamaterial based on negative effective mass density. Phys. Lett. A 2025;531:130151.

[30] Lakes R. Foam structures with a negative poisson's ratio. Science (1979) 1987;235:1038–40.
[31] Huang TT, Ren X, Zeng Y, Zhang Y, Luo C, Zhang XY, Xie YM. Based on auxetic foam: A novel type of seismic metamaterial for Lamb waves. Eng. Struct. 2021;246:112976.
[32] Luo YM, He C, Tao Z, Hao J, Xu HH, Zhang Y, Zhang F, Ren X. A surface-wave seismic metamaterial filled with auxetic foam. Int. J. Mech. Sci. 2024;262:108715.
[33] Li P, Yang F, Zhao M, Du Z, Fan H. A new seismic metamaterial design with ultra-wide low-frequency wave suppression band utilizing negative Poisson's ratio material. Eng. Struct. 2024;319:118821.
[34] Zhao J, Zhou G, Zhang D, Kovacic I, Zhu R, Hu H. Integrated design of a lightweight metastructure for broadband vibration isolation. Int. J. Mech. Sci. 2023;244:108069.
[35] Fang X, Lacarbonara W, Cheng L. Advances in nonlinear acoustic/elastic metamaterials and metastructures. Nonlinear. Dyn. 2024.
[36] Sheng P, Fang X, Yu D, Wen J. Mitigating aeroelastic vibration of strongly nonlinear metamaterial supersonic wings under high temperature. Nonlinear. Dyn. 2024.
[37] LeGrande J, Malla A, Bukhari M, Barry O. Introduction of local resonators to a nonlinear metamaterial with topological features. J. Comput. Nonlinear. Dyn. 2024;19.
[38] Zhang J, Hu G, Tang H, Yang Y. Broadband and tunable vibration suppression via piezoelectric-ABH meta-beam. Int. J. Mech. Sci. 2025;296:110312.
[39] Li Y, Huang Q, Yao S, Shi C. Wave propagation and vibration attenuation in spiral ABH metamaterial beams. Int. J. Mech. Sci. 2024;269:108976.
[40] Sangsefidi A, Younesian D. Enhancement of vibration energy harvesting using a combination of acoustic black holes and meta structures. Mech. Adv. Mater. Struct. 2025:1–20.
[41] Bao Y, Yao Z, Hu X, Liu X, Shan Y, He T. Complete bandgap of three-dimensional helical metamaterial tapered rod with power-law radius. Mech. Syst. Signal. Process. 2024;211:111257.
[42] Mazzotti M, Foehr A, Bilal OR, Bergamini A, Bosia F, Daraio C, Pugno NM, Miniaci M. Bio-inspired non self-similar hierarchical elastic metamaterials. Int. J. Mech. Sci. 2023;241:107915.
[43] Wang Z, Zichao G, Zhendong L, Zeng K. Design, manufacture, and characterisation of hierarchical metamaterials for simultaneous ultra-broadband sound-absorbing and superior mechanical performance. Virtual. Phys. Prototyp. 2023;18:e2111585.
[44] Miniaci M, Krushynska A, Gliozzi AS, Kherraz N, Bosia F, Pugno NM. Design and fabrication of bioinspired hierarchical dissipative elastic metamaterials. Phys. Rev. Appl. 2018;10:024012.
[45] Yang H, Wang B, Ma L. Designing hierarchical metamaterials by topology analysis with tailored Poisson's ratio and Young's modulus. Compos. Struct. 2019;214:359–78.
[46] Ambrosi D, Ben Amar M, Cyron CJ, DeSimone A, Goriely A, Humphrey JD, Kuhl E. Growth and remodelling of living tissues: perspectives, challenges and opportunities. J. R. Soc. Interface 2019;16:20190233.
[47] Lakes R. Materials with structural hierarchy. Nature 1993;361:511–5.
[48] Zhang X, Vyatskikh A, Gao H, Greer JR, Li X. Lightweight, flaw-tolerant, and ultrastrong nanoarchitected carbon. Proc. Natl. Acad. Sci. 2019;116:6665–72.
[49] Zhu S, Wang S, Huang Y, Tang Q, Fu T, Su R, Fan C, Xia S, Lee PS, Lin Y. Bioinspired structural hydrogels with highly ordered hierarchical orientations by flow-induced alignment of nanofibrils. Nat. Commun. 2024;15:118.
[50] Wang G, Cai Z, Deng X. In-plane dynamic impact mechanical properties of novel bi-directional hierarchical honeycomb. Eng. Fract. Mech. 2024;300:110009.
[51] Zhang P, To AC. Broadband wave filtering of bioinspired hierarchical phononic crystal. Appl. Phys. Lett. 2013;102.
[52] Jiang W, Yin G, Xie L, Yin M. Multifunctional 3D lattice metamaterials for vibration mitigation and energy absorption. Int. J. Mech. Sci. 2022;233:107678.
[53] Xu X, Barnhart MV, Li X, Chen Y, Huang G. Tailoring vibration suppression bands with hierarchical metamaterials containing local resonators. J. Sound. Vib. 2019;442:237–48.
[54] Wang G, Lim CW, Chen Z. Lightweight self-similar hierarchical metamaterials with subwavelength and superwide bandgaps. Int. J. Mech. Sci. 2024;280:109527.
[55] Jing J, Sun P, Wu Z, Li F. Investigation on enhanced band-gap properties of 2D hierarchical phononic crystals. Mech. Syst. Signal. Process. 2025;223:111827.
[56] Miniaci M, Kherraz N, Cröenne C, Mazzotti M, Morvaridi M, Gliozzi AS, Onorato M, Bosia F, Pugno NM. Hierarchical large-scale elastic metamaterials for passive seismic wave mitigation. EPJ Appl. Metamat. 2021;8:14.
[57] Pan H, Zhou K. Hierarchical seismic metamaterial design toward enhancing multidirectional seismic attenuation. Mech. Adv. Mater. Struct. 2025:1–17.
[58] Graczykowski B, Alzina F, Gomis-Bresco J, Sotomayor Torres CM. Finite element analysis of true and pseudo surface acoustic waves in one-dimensional phononic crystals. J. Appl. Phys. 2016;119.
[59] Luo YM, Huang TT, Zhang Y, Xu HH, Xie YM, Ren X. Novel meter-scale seismic metamaterial with low-frequency wide bandgap for Lamb waves. Eng. Struct. 2023;275:115321.
[60] Wang Y, Fang Y, Jin-Shui Y, Li-Li T, Qi L, Rüdiger S, Schröder K-U. A new periodic seismic metamaterial with ultra-low bandgap for lamb waves. Mech. Adv. Mater. Struct. 2024;31:7742–52.
[61] Ouakka S, Gueddida A, Pennec Y, Djafari-Rouhani B, Kouroussis G, Verlinden O. Efficient mitigation of railway induced vibrations using seismic metamaterials. Eng. Struct. 2023;284:115767.
[62] Wang Y, Yang F, Yang J-S, Tong L-L, Li S, Liu Q, Hou G-L, Sun P-D, Xing M, Zheng G. Study on vibration damping performance of a petal-shaped seismic metamaterial. Structures 2023;56:104898.
[63] Meade RD, Rappe A, Brommer K, Joannopoulos J, Alerhand O. Accurate theoretical analysis of photonic band-gap materials. Phys. Rev. B 1993;48:8434.
[64] Gao N, Wang B, Lu K, Hou H. Complex band structure and evanescent Bloch wave propagation of periodic nested acoustic black hole phononic structure. Appl. Acoust. 2021;177:107906.
[65] Veres IA, Berer T, Matsuda O. Complex band structures of two dimensional phononic crystals: analysis by the finite element method. J. Appl. Phys. 2013;114.
[66] Guo W, Zhang S-Y, Wang Y-F, Laude V, Wang Y-S. Evanescent Lamb waves in viscoelastic phononic metastrip. Int. J. Mech. Sci. 2022;236:107748.
[67] Miao Z, Li J, Li S, Ma Q. Complex band structure of 2D piezoelectric local resonant phononic crystal with finite out-of plane extension. Appl. Sci. 2022;12:7021.
[68] Oudich M, Assouar MBadreddine. Complex band structures and evanescent bloch waves in two-dimensional finite phononic plate. J. Appl. Phys. 2012;112.
[69] Jiang Y, Meng F, Chen Y, Zheng Y, Chen X, Zhang J, Huang X. Vibration attenuation analysis of periodic underground barriers using complex band diagrams. Comput. Geotech. 2020;128:103821.
[70] Wang G, Wang C, Liang C, Chen Z, Lim CW, Shi Z. Subwavelength partial-embedded seismic metamaterial with wide working frequency: numerical simulation and experiment. Eng. Struct. 2025;332:120093.
[71] Li P, Yang F, Han D, Hou X, Fan H. Application of negative Poisson's ratio materials in pipe seismic metamaterial to achieve low-frequency wide bandgap for surface waves. Eng. Struct. 2025;328:119724.
[72] Liu Z, Qin K-Q, Yu G-L. Partially embedded gradient metabarrier: broadband shielding from seismic rayleigh waves at ultralow frequencies. J. Eng. Mech. 2020;146:04020032.
[73] Gupta A, Sharma R, Thakur A, Gulia P. Metamaterial foundation for seismic wave attenuation for low and wide frequency band. Sci. Rep. 2023;13:2293.
[74] Li L, Wang Q, Liu H, Li L, Yang Q, Zhu C. Seismic metamaterials based on coupling mechanism of inertial amplification and local resonance. Phys. Scr. 2023;98:045024.
[75] Zhang K, Yu J, Liu H, Ding B, Deng Z. Low-frequency and wide bandgap seismic metamaterials for Rayleigh wave attenuation. Eng. Struct. 2023;296:116948.
[76] Zhou W, Zuo H, Bi K, Hao H, Chen W. Bandgap characteristics of a hybrid multi-resonator elastic metamaterial with negative stiffness mechanism and its application to mitigate seismic response of building structures. Thin-Walled Struct. 2024;202:112079.
[77] Palanisamy RP, Chavez LA, Castro R, Findikoglu AT. Void-engineered metamaterial delay line with built-In impedance matching for ultrasonic applications. Sensors 2024;24:995.
[78] Milton GW, Willis JR. On modifications of Newton's second law and linear continuum elastodynamics. Proc. R. Soc. A: Math., Phys. Eng. Sci. 2007;463:855–80.
[79] Du Q, Zeng Y, Huang G, Yang H. Elastic metamaterial-based seismic shield for both Lamb and surface waves. AIP. Adv. 2017;7.
[80] Khelif A, Achaoui Y, Benchabane S, Laude V, Aoubiza B. Locally resonant surface acoustic wave band gaps in a two-dimensional phononic crystal of pillars on a surface. Phys. Rev. B—Cond. Matter Mater. Phys. 2010;81:214303.